NONLINEAR ANALYSIS OF THE SPACE SHUTTLE SUPERLIGHTWEIGHT LO$_2$ TANK: PART II - BEHAVIOR UNDER 3g END-OF-FLIGHT LOADS

Michael P. Nemeth, Richard D. Young, Timothy J. Collins, and James. H. Starnes, Jr.
NASA Langley Research Center
Hampton, Virginia 23681-0001

NONLINEAR ANALYSIS OF THE SPACE SHUTTLE SUPERLIGHTWEIGHT LO₂ TANK: PART II - BEHAVIOR UNDER 3g END-OF-FLIGHT LOADS

Michael P. Nemeth[*], Richard D. Young[†], Timothy J. Collins[‡], and James H. Starnes, Jr.[§]
NASA Langley Research Center
Hampton, Virginia 23681-0001

Abstract

Results of linear bifurcation and nonlinear analyses of the Space Shuttle superlightweight (SLWT) external liquid-oxygen (LO₂) tank are presented for an important end-of-flight loading condition. These results illustrate an important type of response mode for thin-walled shells, that are subjected to combined mechanical and thermal loads, that may be encountered in the design of other liquid-fuel launch vehicles. Linear bifurcation analyses are presented that predict several nearly equal eigenvalues that correspond to local buckling modes in the aft dome of the LO₂ tank. In contrast, the nonlinear response phenomenon is shown to consist of a short-wavelength bending deformation in the aft elliptical dome of the LO₂ tank that grows in amplitude in a stable manner with increasing load. Imperfection sensitivity analyses are presented that show that the presence of several nearly equal eigenvalues does not lead to a premature general instability mode for the aft dome. For the linear bifurcation and nonlinear analyses, the results show that accurate predictions of the response of the shell generally require a large-scale, high-fidelity finite-element model. Results are also presented that show that the SLWT LO₂ tank can support loads in excess of approximately 1.9 times the values of the operational loads considered.

Introduction

The International Space Station (ISS) is currently planned to occupy a 51.6° orbit. Construction of the ISS will require the Space Shuttle to deliver a large number of payloads to this high-inclination orbit. However, achieving this orbit requires that the payload capacity of the orbiter be reduced by approximately 10,000 lb. To recover part of this lost payload capacity, and to minimize the number of Space Shuttle flights needed to build the ISS, the National Aeronautics and Space Administration (NASA) is developing a new lightweight external fuel

---

tank for the Space Shuttle. This new design, referred to as the superlightweight external tank (SLWT), is made primarily of an aluminum-lithium alloy and is expected to weigh approximately 58,000 lb, which is approximately 8,000 lb lighter than the aluminum external tank currently in service. This 8,000 lb weight savings translates into an 8,000 lb increase in the payload capacity for the orbiter.

An important consideration in the design of the SLWT is the nonlinear behavior of its thin-walled regions that experience compressive or shear stresses, and the sensitivity of this behavior to initial geometric imperfections. Small initial geometric imperfections are known to cause premature buckling of thin shell structures. These effects are very important in the present study because local or global buckling of the SLWT shell wall could cause the thermal protection system (TPS) to separate from the tank, which could cause the vehicle to fail. To eliminate shell-wall instabilities from the design, accurate predictions of the nonlinear response and imperfection sensitivity of the SLWT are needed. However, obtaining this information is a significant task. For example, accurate predictions of the nonlinear response of the SLWT have been shown in Ref. 1 to require a large-scale, high-fidelity finite-element model to represent the complex structural details of the SLWT and a robust nonlinear shell analysis capability that can predict local and general instability buckling modes.

One component of the SLWT that experiences significant compressive stresses is the liquid-oxygen (LO₂) tank (see Fig. 1). Prior to launch, the weights of the liquid-hydrogen (LH₂) tank, the LO₂ tank, and the fuel are reacted at the solid-rocket-booster attachment points, which causes meridional compressive stresses and shear stresses that extend into the nose of the SLWT. The nonlinear behavior of the SLWT LO₂ tank subjected to two critical prelaunch loading conditions has been documented extensively in Ref. 1. The tank also experiences similar compressive and shear stresses during ascent, before the two solid rocket boosters (SRBs) are jettisoned. After the SRBs are jettisoned, and prior to orbital insertion, the LO₂ tank experiences compressive stresses in the aft end of the tank instead of the nose region.

The present paper presents results of linear bifurcation and nonlinear analyses of the LO₂ tank that were con-

ducted at the NASA Langley Research Center. The results are for a critical flight loading condition that occurs 423 seconds into the flight, after the SRBs are jettisoned and prior to orbital insertion (referred to herein as the 3g end-of-flight loading condition). First, an overview of the SLWT structure and the details of the loading condition are presented. Then, details of the finite-element model, mesh convergence studies, and load simulation are summarized. Next, details of the linear bifurcation analyses are presented, and then results of nonlinear analyses for geometrically perfect and imperfect shells are presented. The imperfection sensitivity results include a discussion of the effects of modal interactions associated with several nearly equal eigenvalues. Finally, generic aspects of the finite-element model, analyses, and results that may be applicable to the design of future liquid-fuel launch vehicles are discussed.

Overview of the Structure

The Space Shuttle consists of the orbiter, two SRBs, and the external tank (ET), as shown in Fig. 1. The ET consists of a LO_2 tank, a LH_2 tank, and an intermediate structure called the intertank (Fig. 1). The intertank transmits the weight of the fuel, the ET structural weight, and the orbiter weight to the SRBs prior to launch, and transmits thrust loads from the SRBs and the orbiter to the ET during ascent. The SLWT LO_2 tank is a thin-walled monocoque shell that is made primarily of 2195 aluminum-lithium alloy. The LO_2 tank is approximately 49.4 ft long and has a maximum diameter of approximately 27.6 ft, as indicated in Fig. 2. The LO_2 tank consists of a forward ogive section made from eight gore panels, an aft ogive section made from 12 gore panels, a cylindrical barrel section made from four barrel panels, and an aft elliptical dome section made from 12 gore panels. The coordinate systems used to locate the elements of the LO_2 tank and the intertank are also shown in Fig. 2. The coordinates (XT, Y, Z) are typically referred to as the global coordinate system of the ET, and axial positions along the tank are indicated by the coordinate value of XT in units of inches. For example, the location of the junction between the forward and aft ogives is indicated by writing XT = 536.74 in. Cylindrical coordinates are also used and are given by (XT, r, θ), where a positive value of θ is measured from the positive Z-axis toward the positive Y-axis, as shown in Fig. 2b.

The LO_2 tank also has a forward ring frame with a "T"-shaped cross section that is referred to herein as the T-ring frame, and an aft ring frame with a "Y"-shaped cross section that is referred to herein as the Y-ring frame. These two ring frames support a baffle assembly that prevents the fuel from sloshing during ascent. The slosh baffle, a lightweight (approximately 455 lb), thin-
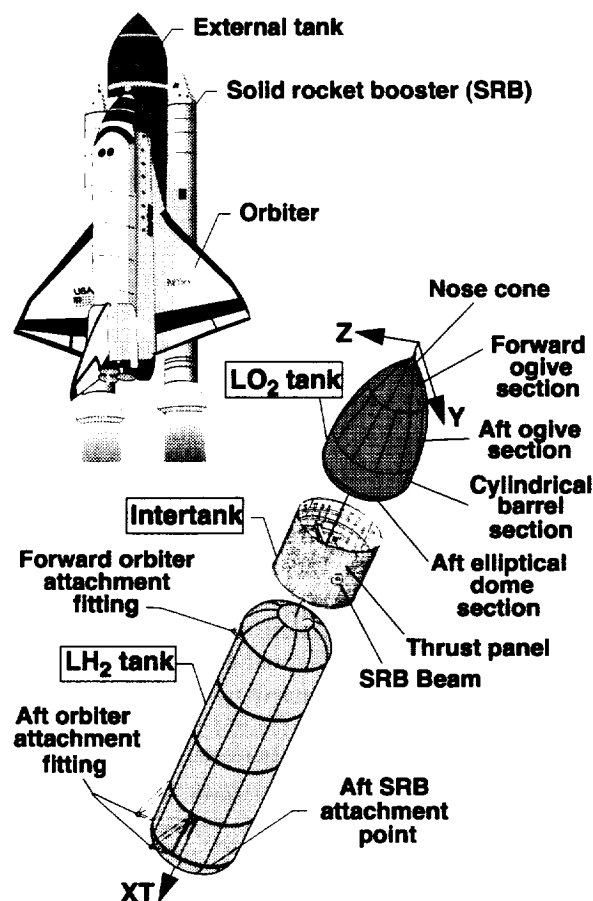

Fig. 1 Space Shuttle External Tank components.

walled structure, is supported by deep, thin-walled rings at each end that attach to the forward T-ring and the aft Y-ring frames. Other parts of the LO_2 tank include a nonstructural nose cone, a forged forward ogive fitting and cover plate, an aft spherical dome cap that contains the LO_2 suction fitting and a covered manhole, and a vortex baffle attached to the base of the aft dome cap. The LO_2 tank gore and barrel panels are stretch formed, chemically milled, and then welded together. The panels are fabricated with substantial thickness tailoring to reduce structural weight. The panels are somewhat thicker at the welds to form a stiffener-like region that is used as a weld land. The primary role of the weld lands is to compensate for any reduction in shell-wall strength that is caused by welding. Tapering the weld lands in thickness and width along their length reduces weight and alleviates stress concentrations in the shell that result from abrupt changes in thickness.

The intertank is a right circular cylinder that is made from 2090 aluminum-lithium and 7075 aluminum alloys and is shown in Fig. 1. The approximately 22.5-ft-long intertank has a diameter of approximately 27.5 ft and consists of six 45° curved panels that are stiffened
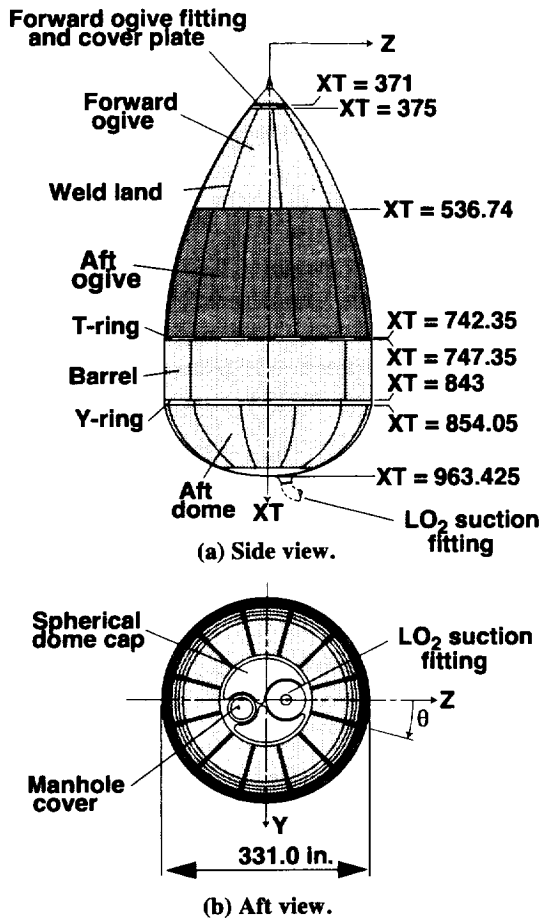
2

Forward ogive fitting
and cover plate

Z

XT = 371
XT = 375

Forward
ogive

Weld land

XT = 536.74

Aft
ogive

T-ring

XT = 742.35

Barrel

XT = 747.35
XT = 843

Y-ring

XT = 854.05

XT = 963.425

Aft
dome XT

LO$_2$ suction
fitting

(a) Side view.

Spherical
dome cap

LO$_2$ suction
fitting

Z
θ

Manhole
cover

Y

331.0 in.

(b) Aft view.

Fig. 2 Space Shuttle External LO$_2$ Tank components (values of XT given in inches).

longitudinally with external hat stiffeners and are referred to herein as skin-stringer panels. The intertank also has two massive 45° curved panels, referred to as thrust panels (see Fig. 1), that are located perpendicular to the Y-axis of the intertank and stiffened longitudinally with integrally machined external blade stiffeners. These eight panels are assembled into the intertank with mechanical fasteners and are attached to five large internal ring frames, a forward flange, and an aft flange. Longitudinal straps (referred to herein as roll ties) suppress lateral-torsional deflection of the ring frames. The main central ring frame, two thrust panel longerons, and the thrust panels are connected to each end of a tapered beam that is referred to herein as the SRB beam (see Fig. 1). The SRB beam spans the diameter of the intertank along the Y-axis and has a maximum depth (in the XT direction) of approximately 43 in. at its midspan. Forged fittings (referred to herein as SRB thrust fittings) that are incapable of transmitting moments are fastened to the ends of the SRB beam. The primary role of the thrust panels is to diffuse the large axial loads introduced by the SRBs into the intertank and then into the LO$_2$ tank shell

wall. The SRB beam compensates for the eccentricity of the concentrated loads introduced by the SRBs. The SRB beam also supports loads that are normal to the intertank (parallel to the SRB beam) at the SRB attachment points. The intertank also has a 46-in.-high by 52-in.-wide frame-reinforced nonstructural access door located along the cylinder generator at approximately $\theta = 146°$.

Critical Loading Condition

The 3g end-of-flight loading condition was identified by the members of the SWLT team at the NASA Marshall Space Flight Center and the Lockheed Martin Manned Space Systems Company as a critical loading condition that could cause buckling of the aft dome of the LO$_2$ tank. This critical loading condition corresponds to a partially filled LO$_2$ tank aft dome and an acceleration field given by $a_X = -3.040g$, $a_Y = 0.005g$, and $a_Z = -0.725g$, where g is the magnitude of the gravitational acceleration. The X subscript in the first acceleration corresponds to the XT direction and is used in the present paper for convenience. Details of this loading condition are shown in Figs. 3 and 4. The loads consist of the inertial loads of the structural mass and the LO$_2$ mass, the ullage pressure exerted on the shell wall (see Fig. 4), the LH$_2$ tank interface force and moment, and the thermal load associated with the cryogenic fuel and aerodynamic heating. No SRB forces or aerodynamic pressure loads are present for this loading condition because the SRBs have been jettisoned by this point in the flight profile and the orbiter and external tank are essentially out of the
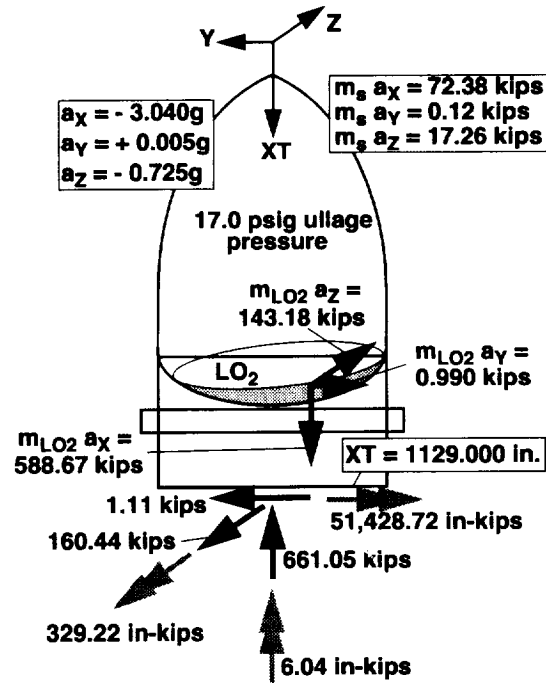

Y   Z

$a_X = -3.040g$
$a_Y = +0.005g$
$a_Z = -0.725g$

XT

$m_s \, a_X = 72.38$ kips
$m_s \, a_Y = 0.12$ kips
$m_s \, a_Z = 17.26$ kips

17.0 psig ullage
pressure

$m_{LO2} \, a_Z = 143.18$ kips

$m_{LO2} \, a_Y = 0.990$ kips

LO$_2$

$m_{LO2} \, a_X = 588.67$ kips

XT = 1129.000 in.

1.11 kips

160.44 kips

51,428.72 in-kips

661.05 kips

329.22 in-kips

6.04 in-kips

Fig. 3 Loads at 423 seconds into flight.

3

dense part of the Earth's atmosphere. The inertial loads of the structural mass (magnitudes) are given by $m_s\, a_X$ = 72.38 kips, $m_s\, a_Y$ = 0.12 kips, and $m_s\, a_Z$ = 17.26 kips. Similarly, the inertial loads of the LO_2 mass are given by $m_{LO2}\, a_X$ = 588.67 kips, $m_{LO2}\, a_Y$ = 0.99 kips, and m_{LO2} a_Z = 143.18 kips (see Fig. 3). The interface force and moment between the intertank and the LH_2 tank are given by $\mathbf{F}$ = $-$ 661.050$\mathbf{i}$ + 1.110$\mathbf{j}$ -160.440$\mathbf{k}$ kips and $\mathbf{M}$ = $-$ 6.040$\mathbf{i}$ - 51,428.720$\mathbf{j}$ -329.220$\mathbf{k}$ in-kips, where $\mathbf{i}$, $\mathbf{j}$, and $\mathbf{k}$ are standard orthonormal base vectors associated with the XT, Y, and Z axes, respectively.

As the ET is accelerated, the LO_2 mass exerts pressure on the LO_2 tank shell wall. The resultant force of this pressure distribution corresponds to the inertial loads of the LO_2 that are given in Fig. 3. This pressure distribution is approximated by the situation depicted in Fig. 4 in which the LO_2 and its container are subjected to rigid-body motion and flow effects are neglected. This approximate pressure distribution is given by
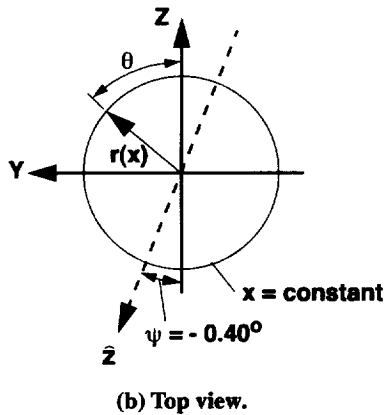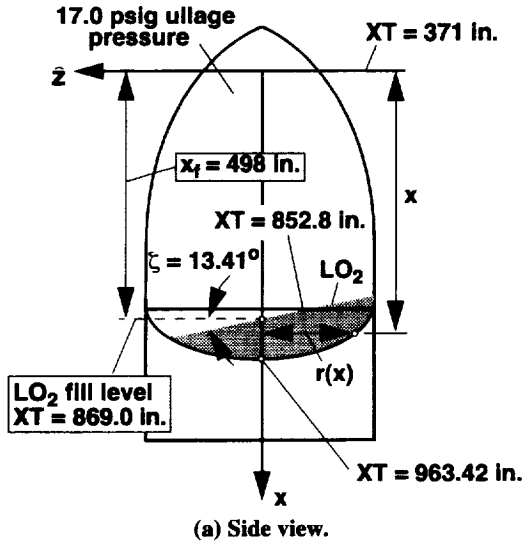

17.0 psig ullage pressure

XT = 371 in.

$\hat{z}$

$x_f = 498$ in.

XT = 852.8 in.

$\zeta = 13.41^\circ$

LO_2

$r(x)$

LO_2 fill level XT = 869.0 in.

XT = 963.42 in.

x

(a) Side view.

Z

θ

Y

$r(x)$

x = constant

$\psi = -0.40^\circ$

$\hat{z}$

(b) Top view.

Fig. 4 LO_2 pressure distribution at 423 seconds into flight.

$$p(x,\theta) = p_u \text{ for } x \le x_f \pm r(x)\left(\frac{a_Y}{a_X}\sin\theta + \frac{a_Z}{a_X}\cos\theta\right) \text{ and}$$

$$p(x,\theta) = p_u \pm \gamma_{LO2}\left|\frac{a_X}{g}\left(x \pm x_f\right) + r(x)\left(\frac{a_Y}{g}\sin\theta + \frac{a_Z}{g}\cos\theta\right)\right|$$

for $x > x_f \pm r(x)\left(\frac{a_Y}{a_X}\sin\theta + \frac{a_Z}{a_X}\cos\theta\right)$ where x is a local axial coordinate that is measured from XT = 371.00 in., x_f = 498 in. is the local x-coordinate of the fill level (XT = 869.00 in.), and r(x) is the horizontal or polar radius of the tank. The ullage pressure is given by p_u = 17.0 psig and the specific weight of the LO_2 that was used in the present study is given by γ_{LO2} = 0.04123 lb/in^3. The local $\hat{z}$-axis shown in Fig. 4 corresponds to the axis of maximum inclination of the free surface of the LO_2 and is given by $\theta = 180^\circ + \psi$, where $\psi = \mathrm{Tan}^{\pm 1}(a_Y/a_Z)$ = $-$ 0.40°. Similarly, the free surface of the LO_2 has an inclination angle in the x-$\hat{z}$ plane that is given by

$$\zeta = \mathrm{Tan}^{\pm 1}\left[\sqrt{a_Y^2 + a_Z^2}\,/\,|a_X|\right] = 13.41^\circ.$$

The temperature distribution that was used in the present study as an approximation associated with the cryogenic fuel and aerodynamic heating is shown in Fig. 5. The temperature distribution shown in this figure is axisymmetric and varies along the surface meridians in a piecewise-linear manner. The hottest place on the LO_2 tank and the intertank is the tip of the ogive (275 $^\circ$F), and the coldest is at the bottom region of the aft dome (-297 $^\circ$F). The nominal ambient temperature of the LO_2 tank and the intertank prior to fueling is 50 $^\circ$F. This temperature was used in the present study as the temperature at which thermal stresses in the LO_2 tank are absent.

Analysis Code and Finite-Element Modeling

The results of the linear bifurcation buckling and nonlinear analyses were obtained with the STructural Analysis of General Shells (STAGS) nonlinear structural analysis code for general shells.[2] The finite-element models of the SLWT tank that were used in the present study are very complex and include many structural details and the skin thickness variations or tailoring used to reduce structural weight. A detailed description of these models is presented in Ref. 1. STAGS was chosen for analyzing the SLWT tank because of its robust state-of-the-art nonlinear-equation solution algorithms and its general user-input capability that is convenient for modeling branched shells typically used for launch vehicles. In particular, STAGS uses both the full and modified Newton methods to obtain an accurate nonlinear solution, and large rotations in the shell are represented by a co-rotational algo-
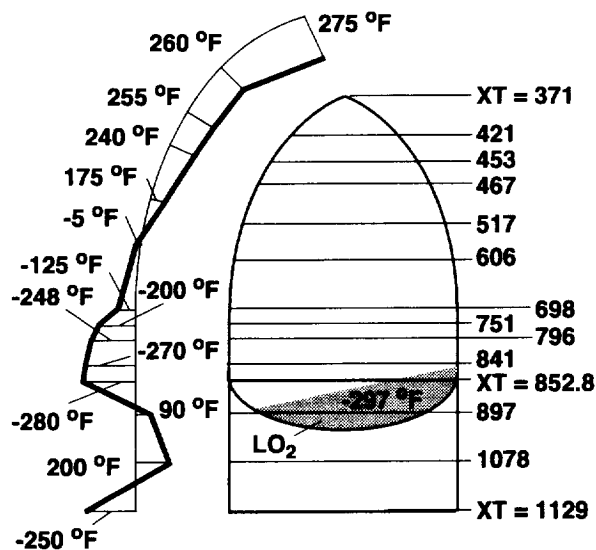
4

Fig. 5 Axisymmetric temperature profile at 423 seconds into flight (values of XT are given in in.).

rithm at the element level. The Riks arc-length projection method is used to continue a solution past limit points. STAGS permits complex geometries, loading conditions, and initial geometric imperfections to be modeled in a direct manner by the use of user-written subroutines that are essentially independent of the mesh discretization. For example, these user-written subroutines allow the user to define reference surface geometries; tapered shell walls and stiffener cross-sections; and complex nodal force, temperature, and pressure distribution functions in a direct manner, using the FORTRAN computer language. This feature greatly simplified the definition of the finite-element models and the mesh convergence studies conducted in the present study. A description of how the features of STAGS were used in the present study to model the SLWT LO$_2$ tank and intertank, and details of how applied prelaunch loads were simulated are presented in Ref. 1.

The basic approach used in the present study to simulate the actual 3g end-of-flight loading condition is to apply all accelerations and associated inertial and LO$_2$ pressure loads illustrated in Figs. 3 and 4 to the model. The thermal load was applied by introducing the axisymmetric temperature distribution shown in Fig. 5 as a temperature change from a nominal initial uniform temperature of 50°F. The bottom of the intertank, where the LH$_2$ tank interface force and moment act, was restrained so that the LH$_2$ tank interface force and moment become reactions, and rigid body motion is eliminated. Next, the applied loads were separated into two groups. The first group contains the pressure that acts on the shell wall because of the acceleration of the LO$_2$ mass, the structural-mass inertial loads, and the inertial line loads that represent the acceleration of the slosh baffle mass

that is located inside of the barrel section of the LO$_2$ tank. This group of loads is treated as the primary source of destabilizing compressive stresses in the LO$_2$ tank that may occur at load levels greater than the corresponding operational load level. The second group of loads consists of the thermal load and the LO$_2$ tank ullage pressure. The loads in the second group are constant in value, are part of the operational loads, and are considered to be passive loads when determining the stability margin of safety of the LO$_2$ tank. In performing linear bifurcation buckling and nonlinear analyses with STAGS, two load factors, p_a and p_b, were assigned to the first (active) and second (passive) load groups, respectively. Values of $p_a = p_b = 1$ correspond to the loading condition that was mentioned previously as the operational load level.

In modeling the SLWT LO$_2$ tank and the intertank, several assumptions were made to simplify the finite-element models. Limited parametric studies were conducted to determine the adequacy of the assumptions and simplifications. For each case in these studies, the modeling assumptions used to simplify the finite-element models were found to be acceptable for analyzing the nonlinear behavior of the SLWT LO$_2$ tank. In addition, the finite-element modeling approach that was used for the SLWT LO$_2$ tank was also applied for the analysis of two full-scale structural tests that were conducted at the NASA George C. Marshall Spaceflight Center on the original standard weight ET during the development program of the original Space Shuttle ET. The analytical results for these two test articles, which buckled unexpectedly during the tests, indicate that the finite-element modeling approach that is used in the present study is adequate for representing the nonlinear behavior of the SLWT LO$_2$ tank (Ref. 1).

Results and Discussion

Three different finite element models were used in the present study for analysis of the LO$_2$ tank subjected to the 3g end-of-flight loading condition. As a first step toward identifying an adequate model with as few degrees of freedom as necessary, linear bifurcation buckling analyses were conducted. The passive loads associated with load factor p_b were applied to the STAGS models as a linear prebuckling stress state ($p_b = 1$) and the active (destabilizing) loads associated with load factor p_a were used to obtain the minimum eigenvalue. The models that were investigated had 76,900, 103,400, and 158,000 degrees of freedom. The model that was identified as adequate for predicting the linear bifurcation buckling behavior is shown in Fig. 6 and corresponds to 158,000 degrees of freedom.

The first linear bifurcation mode (referred to herein as the linear bifurcation buckling mode) for the geometrically perfect shell is shown in Fig. 7 for the STAGS mod-

(a) Mesh with intertank shown.
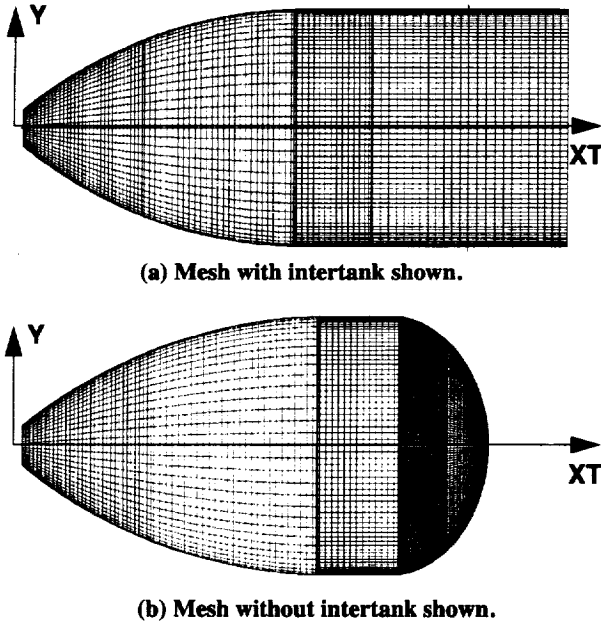

(b) Mesh without intertank shown.

Fig. 6 Finite element mesh (158,000 degrees of freedom).

el with 158,000 degrees of freedom. The eigenvalue for this model corresponds to active loads that are approximately 1.526 times the magnitude of the corresponding operational loads shown in Figs. 3 and 4. This buckling mode is a localized, short-wavelength wrinkle in the forward part of the aft dome that extends from approximately $\theta = 98°$ to $132°$ with its large amplitude region centered approximately on $\theta = 112.5°$. The second through fourth linear bifurcation modes are also localized, short-wavelength modes, similar to the mode shown in Fig. 7, with eigenvalues equal to 1.528, 1.540, and 1.541, respectively, which are all less than 1% higher than the lowest eigenvalue. The second linear bifurcation mode, which is nearly identical to the first mode, is also in the forward part of the aft dome with its large amplitude region centered very close to $\theta = 112.5°$. The third and fourth modes are also nearly identical and located in the forward part of the aft dome, but their large amplitude regions are centered approximately on $\theta = 247.5°$.

The nearly equal values of the first four eigenvalues, the short wavelength of the linear bifurcation modes, and the large difference in location between the first two and last two linear bifurcation modes led to the dense mesh refinement of the aft dome that is shown in Figs. 6 and 7. A uniform circumferential mesh refinement of the dome was used in order not to bias the location of the response, and was facilitated by the use of the five-node and seven-node rectangular transition elements available in STAGS.[3] The 103,400- and 158,000-degree-of-freedom models have the same general mesh arrangement shown in Fig. 6, but the level of refinement of the forward part of the aft dome shown in Figs. 6 and 7 for the 158,000-de-
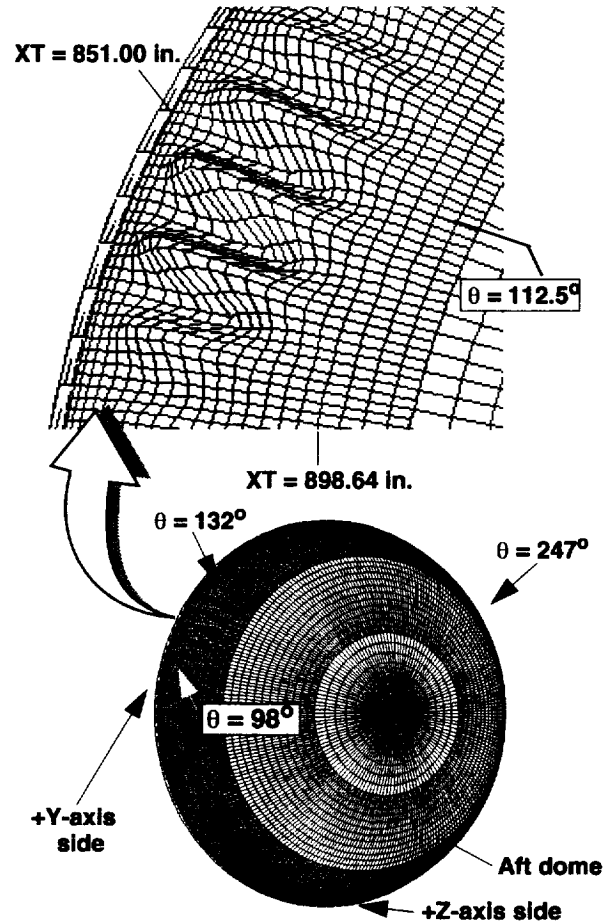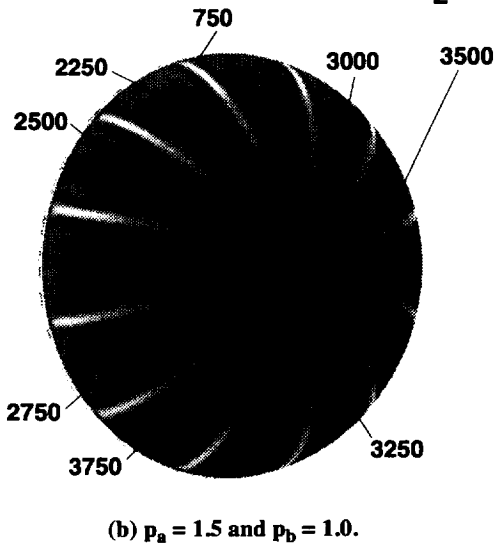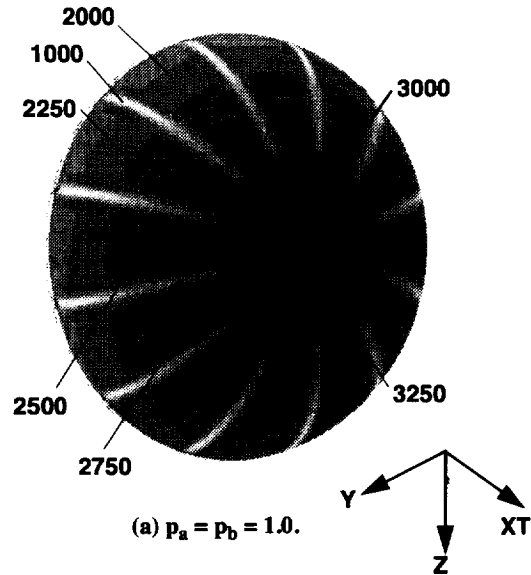

Fig. 7 Linear bifurcation buckling mode (158,000 degrees of freedom; $p_a = 1.526$ and $p_b = 1.0$).

gree-of-freedom model is essentially twice that of the 103,400-degree-of-freedom model. The lowest eigenvalues for the 103,400- and 158,000-degree-of-freedom models are given by $p_a = 1.536$ and $p_a = 1.526$, respectively. The smoothness of the buckling mode shown in Fig. 7 and the one-percent difference in the eigenvalues, suggest that the 158,000-degree-of-freedom model is adequate for representing the linear bifurcation behavior of the LO_2 tank for this loading condition. The 103,400- and 158,000-degree-of-freedom models were also used to obtain nonlinear solutions for geometrically perfect and imperfect shells. These solutions, which are in good agreement, indicate that the 158,000-degree of freedom model adequately represents the nonlinear behavior of the LO_2 tank for this loading condition. Thus, all subsequent results presented in this section were obtained with the 158,000-degree-of-freedom model.

The meridional stress resultant distribution (given in units of lb/in.) in the aft dome, that was obtained from nonlinear analyses, is tensile and is shown in Fig. 8 for values of $p_a = p_b = 1$ and for $p_a = 1.5$ and $p_b = 1$. The lighter meridional bands of shading shown in the figure
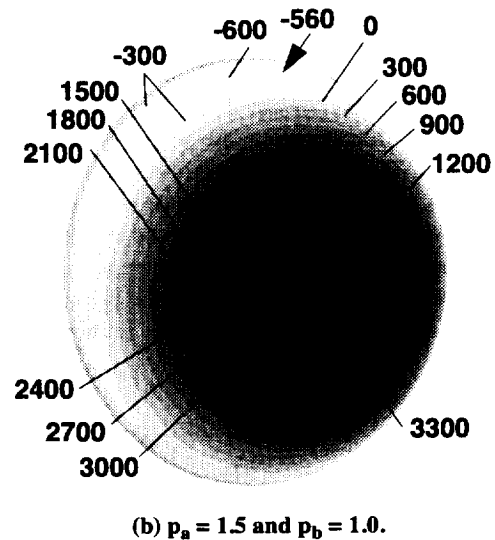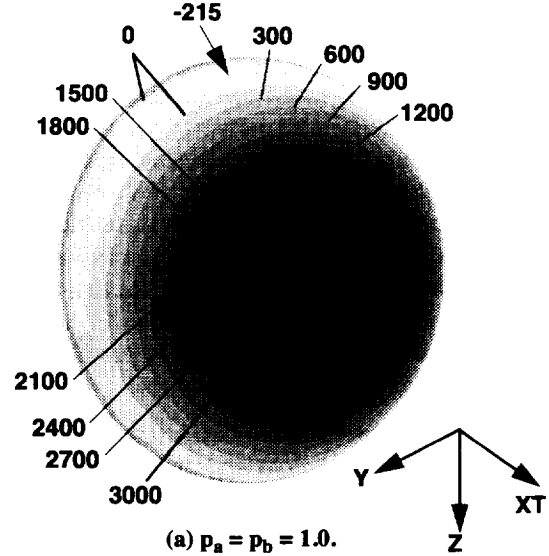
6

(a) $p_a = p_b = 1.0$.

(b) $p_a = 1.5$ and $p_b = 1.0$.

Fig. 8 Meridional stress resultants in aft dome (lb/in.).

(a) $p_a = p_b = 1.0$.

(b) $p_a = 1.5$ and $p_b = 1.0$.

Fig. 9 Circumferential stress resultants in aft dome (lb/in.).

correspond to lower values of the meridional stress resultants along the weld lands. The meridional tension shown in the figure primarily resists the axial acceleration of the LO_2 mass and is responsible for the shortness of the wavelength of the linear bifurcation buckling mode. The circumferential stress resultants in the aft dome that generate the linear bifurcation modes are shown in Fig. 9 for values of $p_a = p_b = 1$ and for $p_a = 1.5$ and $p_b = 1$. These results show a region of circumferential compression ($90° \le \theta \le 270°$) that is also in the forward part of the aft dome, with the highest values of compression approximately near $\theta = 180°$. The average shell wall thickness in and around this region is 0.090 in.

An important concern that arose during the course of the present study is the possiblity of high sensitivity to initial geometric imperfections, that may be caused by the presence of four closely spaced eigenvalues of the linear bifurcation modes. This sensitivity could lead to a premature collapse mode of the aft dome. This concern led to the use of an imperfection shape that is in the form of a linear combination of the first four linear bifurcation modes, described previously in the present paper, in the nonlinear analyses of the imperfect shell. With this four-mode imperfection each mode possesses an equal degree of participation. Mathematically, this set of modes can be viewed loosely as a basis for an "isotropic imperfection space," similar to a basis of a vector space. The first four modes were selected because they represent deformation states that the structure has an intrinsic affinity to deform into, provided that there are no substantial nonlinear pre-buckling effects present. That is, in the absence of sub-

7

stantial nonlinear prebuckling effects, the linear
bifurcation eigenvalues represent when (at what load lev-
el) and where (what configurations) strong interactions
between compressive membrane stresses and normal dis-
placements are likely to be present. In addition, the four-
mode imperfection was selected because of the statement
given by Bushnell[4] that suggests that premature failure of
shell structures that exhibit a short-wavelength response
can be activated or "triggered" by imperfections with a
similar short-wavelength shape. Thus, the four-mode im-
perfection is expected to represent adequately a preferred
direction of departure from the primary equilibrium path
should the structure have a tendency to do so.

Results are presented in Figs. 10 and 11 that show
the nonlinear deformations that were obtained from
STAGS analyses of a geometrically perfect shell and a
geometrically imperfect shell with an imperfection-am-
plitude-to-wall-thickness ratio $A/t = 1$, respectively. The
thickness t in the ratio A/t is the average wall thickness
of the top part of the aft dome (t = 0.090 in.). The results
shown in Fig. 11 were obtained by using the four-mode
imperfection that was described previously in the present
paper. For this imperfection, the imperfection shape is
given by -0.707 times the summation of the first four
eigenvectors. The negative of the linear combination was
used as the imperfection shape because it was found to
provide a stronger nonlinear interaction with the com-
pressive stresses in the shell wall than the positive-valued
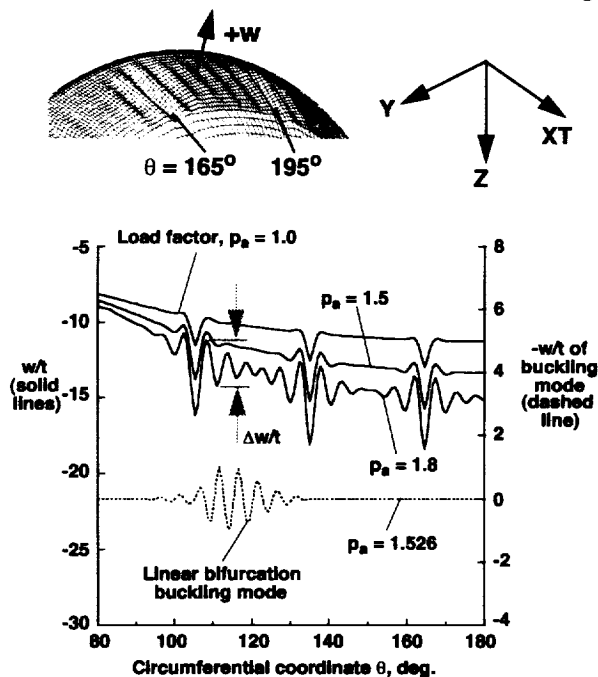linear combination. The results shown in these two fig-

Fig. 10 Nondimensional normal displacement w/t of
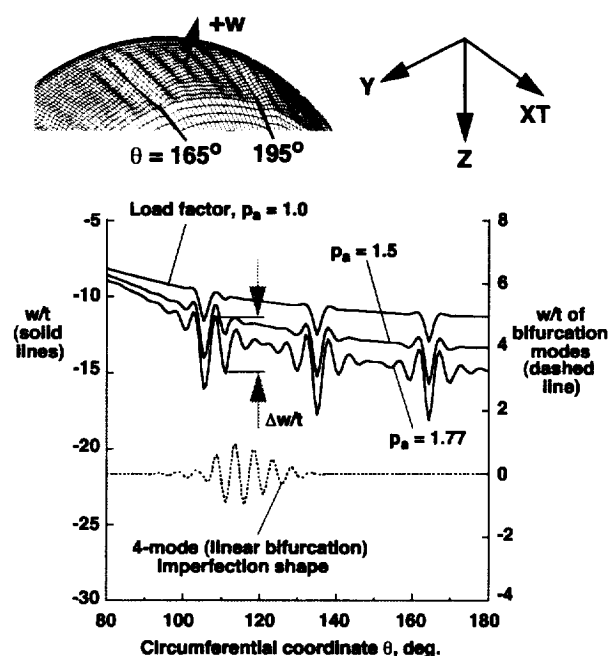geometrically perfect aft dome (t = 0.090 in.; XT = 885
in.).

Fig. 11 Nondimensional normal displacement w/t of
geometrically imperfect aft dome. (Imperfection-
amplitude-to-wall-thickness ratio A/t = 1; t = 0.090 in.;
XT = 885 in.).

ures are for nonlinear solutions that were obtained by in-
creasing the load factors p_a and p_b simultaneously to a
value of one, and then holding p_b constant while increas-
ing the magnitude of the load factor p_a. The nondimen-
sional normal displacements w/t along the circumference
of the aft dome shell wall at XT = 885 in. and from θ =
80° to 180° are represented by the solid lines in the fig-
ures for values of the load factor p_a approximately equal
to 1.0, 1.5, and 1.8. Moreover, the line given by θ = 180°
in each figure is essentially a line of reflective symmetry
for the nonlinear-response curves. Overall, negative val-
ues of the normal displacements are indicated by the left-
hand ordinate for these three load factors. These results
are negative because of the contraction of the aft dome
that is caused primarily by the LO_2 thermal load (shrink-
age). The linear bifurcation buckling mode and half of
the four-mode imperfection are represented by the dashed
lines in Figs. 10 and 11, respectively, with normalized
amplitudes given by the right-hand ordinate of the fig-
ures. The third linear bifurcation mode is obtained by re-
flection of the dashed line in Fig. 10 about the line θ =
180°. Similarly, the second half of the four-mode imper-
fection is obtained by reflection of the dashed line in Fig.
11 about the line θ = 180°. The linear bifurcation buck-
ling mode and the half of the four-mode imperfection
shown in the figures are very similar and are included in
the figures to give an indication of how the imperfection
shape influences the nonlinear solution.

The solid lines shown in the Figs. 10 and 11 indi-

8

cate a short-wavelength bending response in the circumferentially compressed part of the aft dome that extends from approximately $\theta = 95°$ to $180°$. Although they are not shown in the figures, the deformations are symmetric about the right-hand axis and actually extend to approximately $\theta = 265°$. The pattern of the nonlinear deformations are substantially different from the linear bifurcation buckling mode and the four-mode imperfection, and encompass a much larger portion of the dome circumference. The overall increasing slope trend of the solid lines in the figures (seen by neglecting the undulations in the curves) is due to the inward displacement of the shell wall that is caused by the increase in pressure and temperature change as p_a and p_b are simultaneously increased to a value of one in the nonlinear analysis. This effect is not accounted for in a linear bifurcation buckling analysis and, as a result, the dashed lines do not exhibit a similar overall increasing slope trend.

The results presented in Figs. 10 and 11 predict a stable, but highly wrinkled, nonlinear response at a load level greater than the load level predicted by the linear bifurcation buckling analysis ($p_a = 1.526$). At the operational load level given by $p_a = 1$, the results predict significant nonlinear prebuckling deformations at values close to $\theta = 105°, 135°,$ and $165°$ which are the locations of the meridional weld lands in that part of the aft dome. As the load is increased, substantial bending deformations (indicated by the waviness of the curves) develop and grow in the shell wall between the weld lands, which reduces the apparent circumferential stiffness of the aft dome. The largest bending deformations shown in the figures are predicted to occur at the locations of the meridional weld lands and are thought to be slightly overpredicted because the weld lands are represented by discrete stringers (concentrated stiffnesses). Although it is difficult to see in the figures, these results also indicate that a geometrical imperfection in the shape of the first four linear bifurcation modes and with a small negative amplitude does amplify the severity of the bending deformations (e.g., compare the magnitudes of $\Delta w/t$ shown in the figures) and causes the growth of the bending deformations to start at slightly lower load levels.

The reduction in the apparent circumferential stiffness of the aft dome is shown more explicitly in Figs. 12 and 13 for the geometrically perfect and imperfect shells, respectively. In these figures, the intensities of the bending deformations along $XT = 885$ in., that are shown in Figs. 10 and 11, are given as a function of the load factor p_a for several circumferential locations. The intensity of the bending deformations is given by the nondimensional quantity $\Delta w/t$, which is the normalized amplitude of an undulation in the curves at a specific value of θ. For example, $\Delta w/t$ is shown in Figs. 10 and 11 for approximately $\theta = 110°$. Four curves are presented in Fig. 12
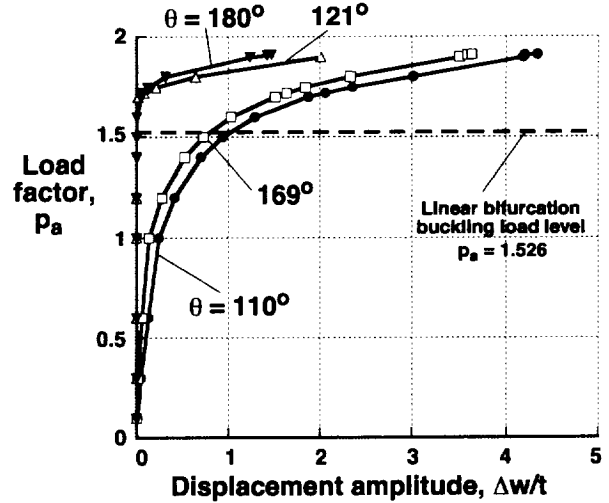

Fig. 12 Local nondimensional normal displacement amplitudes $\Delta w/t$ of geometrically perfect aft dome at $XT = 885$ in. ($t = 0.090$ in.).

for the geometrically perfect shell that correspond to values of $\theta = 110°$(filled circles), $121°$(unfilled triangles), $169°$(unfilled squares), and $180°$(filled triangles). The curves for $\theta = 110°$ and $169°$ correspond to the severe bending deformations next to two of the weld lands, and the other two curves correspond to locations that are approximately midway between weld lands. Similarly, the curves for $\theta = 110°$ and $180°$ that are shown in Fig. 12 are also shown in Fig. 13 (solid curves) along with the corresponding curves for the imperfect shell with $A/t = 1$ (dashed curves). The horizontal dashed lines shown in Figs. 12 and 13 represent the linear bifurcation buckling load level ($p_a = 1.526$).
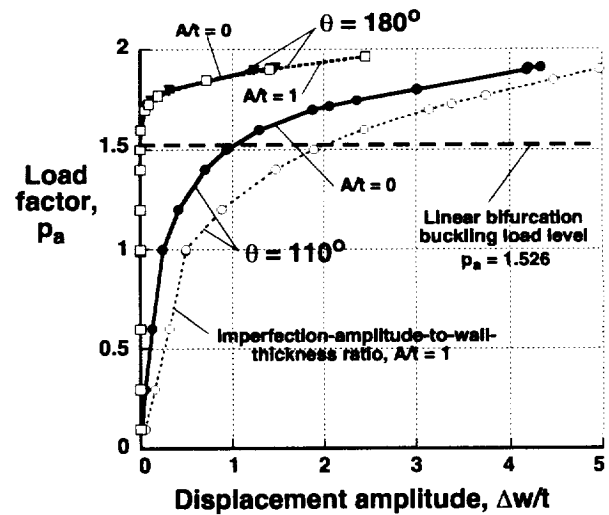
The results shown in Figs. 12 and 13 indicate that

Fig. 13 Local nondimensional normal displacement amplitudes $\Delta w/t$ of geometrically perfect and imperfect aft domes at $XT = 885$ in. ($t = 0.090$ in.).

9

the bending deformations near the meridional weld lands dominate the response of the aft dome; that is, $\Delta w/t$ grows at the highest rate at $\theta = 110°$ and $169°$. Moreover, the results predict that this effect is much more pronounced for the imperfect shell with $A/t = 1$. The curves for $\theta = 110°$ were included in Fig. 13 because they show the greatest effect of the four-mode imperfection. In contrast, the effect of the imperfection is shown to be benign for the point between weld lands at $\theta = 180°$. Corresponding results were obtained for $\theta = 121°$ and $169°$. These results show that the effect of the imperfection at $\theta = 121°$ (between weld lands) was slightly larger than that shown in Fig. 13 for $\theta = 180°$, but much smaller than that shown for $\theta = 110°$ (next to a weld land). Also, the results show that the effect of the imperfection at $\theta = 169°$ (next to a weld land) is benign.

All the results shown in Figs. 12 and 13 show a monotonically increasing nonlinear response and predict that the shell can support loads greater than the critical buckling load predicted by a linear bifurcation buckling analysis. As $\Delta w/t$ increases, the apparent circumferential stiffness decreases, and as a result, the positive-valued constant of proportionality between an increment in load and the corresponding increment in displacement amplitude decreases. This trend is manifested by the reduction in slope of the load versus displacement amplitude curves. This type of response is similar to the response presented for the prelaunch loading condition with full LO_2 and LH_2 tanks,[1] and to the response reported by Stevens, Starnes, and Almroth[5] for cylindrical shells subjected to combined internal pressure and a pure bending moment. The results in Ref. 5 indicate that the amplitude of the short-wavelength deflection grows rapidly as the load increases and approaches a critical value. At the critical value of the load, the load-deflection response curve approaches a horizontal tangent that corresponds to a local collapse mode of the cylinder. Mathematically, the horizontal tangent indicates that unbounded growth of the displacement occurs for an infinitesimal increase in the load. It is expected that the curves shown in Figs. 12 and 13 would approach a horizontal tangent as $\Delta w/t$ increases until a redistribution in load occurs within the aft dome. As a horizontal tangent in a load versus displacement amplitude curve is approached, the region of the shell containing the bending deformations becomes incapable of supporting additional load, and the compressive load is redistributed to another portion of the aft dome. If other parts of the dome cannot support the redistributed compressive load or if excessive yielding occurs, the shell will collapse.

The results presented in Figs. 10 through 13 indicate that large local bending deformations may occur in the shell wall for loads that are much smaller than the local collapse load and may cause the thermal protection

system (TPS) to debond from the shell wall and fail. This mode of failure is of great importance in the design of the TPS for contemporary space vehicles. The results presented in Fig. 14 give approximate estimates of the local radius of curvature ρ for the bending deformation in the aft dome at $XT = 885$ in. and $\theta = 109°$ (next to a weld land). The local radius of curvature ρ was calculated with STAGS as close as possible to the crests of the deformations patterns where the slope $w' = 0$. At this location, the radius of curvature is given by $\rho = |w''|^{\pm 1}$, where w is the normal displacement and the prime marks in the equation denote differentiation with respect to a local Cartesian surface coordinate. The filled circles shown in the figure correspond to results for the geometrically perfect shell, and the unfilled circles correspond to results for the geometrically imperfect shell with imperfection-amplitude-to-wall-thickness ratios of $A/t = 1$. The results in Fig. 14 demonstrate that the geometric imperfection amplitude has a significant influence on the local radius of curvature of the shell wall. For example, if a given thermal protection system is known to debond from the shell wall at a value of $\rho = 100$ in., the maximum load factor is reduced from a value of approximately 1.6 for the geometrically perfect shell to 1.3 for the geometrically imperfect shell with $A/t = 1$. However, a large amplitude, short-wavelength imperfection of this type is very unlikely to be present in a piece of high-precision flight hardware. Thus, the radius-of-curvature results for the perfect shell are much more practical than the corresponding results for the imperfect shell since such large imperfections would most likely be identified during inspection of the shell.

Despite the concerns about acute imperfection sensitivity that is sometimes associated with the presence of several nearly equal linear bifurcation eigenvalues, the re-
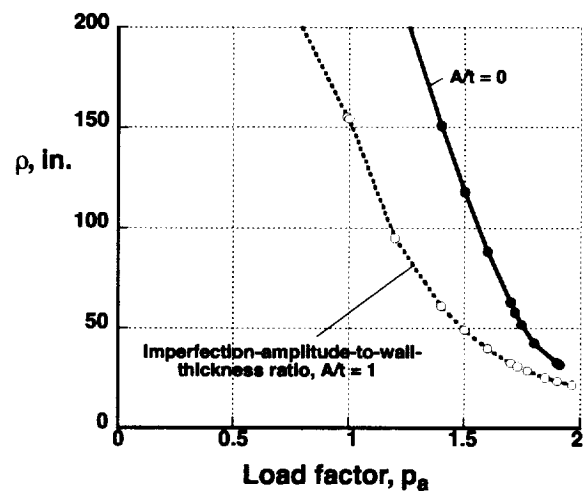

Fig. 14 Local radii of curvature ρ of bending deformation at $XT = 885$ in. and $\theta = 109°$ for geometrically perfect and imperfect aft domes ($t = 0.090$ in.).

10

sults presented in Figs. 10 through 13 indicate a stable nonlinear response for the imperfect shell, which has a relatively large imperfection amplitude. Moreover, the results indicate the presence of substantial nonlinear prebuckling deformations that appear to diminish the significance of the closely spaced linear bifurcation eigenvalues. This trend is consistent with the qualitative guidelines for imperfection sensitivity given in Ref. 4. The trend can be explained by noting that, as the nonlinear prebuckling deformations grow with increasing load, they represent a perturbation of the shell geometry and a local change in the stress state that is not represented physically by the linear bifurcation eigenvalues. The stability of the wrinkle-like deformation state is at least partially attributed to the fact that the compression region is a local region that is more likely to cause a benign internal load redistribution in the presence of nonlinear prebuckling deformations than a sudden mode change or collapse. This explanation is consistent with qualitative guidelines for imperfection sensitivity that are presented in Ref. 4 and was confirmed in the analyses by performing bifurcation analyses from the nonlinear configurations at several of the higher load levels. The behavior of the aft dome of the LO_2 tank is significantly different from that of a compression-loaded cylinder or an externally pressurized sphere which exhibit several nearly equal, or a multiplicity of, linear bifurcation eigenvalues. A major difference is that the region of compression of the aft dome does not fully envelop the shell, unlike the compression-loaded cylinder or the externally pressurized sphere. This difference facilitates load redistribution in the aft dome without shell collapse or a mode change.

Concluding Remarks

Linear bifurcation and nonlinear analyses of the Space Shuttle superlightweight (SLWT) liquid-oxygen (LO_2) tank have been presented. The loading details for an important end-of-flight-loading condition have been described and the analytical method used to simulate the loading condition has been discussed. Results have been presented herein that were obtained from complex, large-scale finite-element models of a portion of the Space Shuttle SLWT. These results illustrate an important type of nonlinear response for thin-walled shells, that are subjected to combined mechanical and thermal loads, that may be encountered in the design of other liquid-fuel launch vehicles. In addition, the results indicate that large-scale, high-fidelity finite-element models are generally required to predict accurately the linear bifurcation and nonlinear responses.

For the end-of-flight-loading condition, linear bifurcation analyses yielded several nearly equal eigenvalues that correspond to local buckling modes. However,

the nonlinear analyses yielded a response that is characterized by a short-wavelength bending deformation that grows in amplitude in a stable manner with increasing load. These local bending deformations appear in the aft elliptical dome of the LO_2 tank and do not lead to a general instability mode, but may cause failure of the thermal protection system (TPS). Because of this concern, results have been presented that can be used to determine the load level at which a TPS failure is likely to occur. Imperfection sensitivity analyses have also been presented that indicate that the aft dome does not exhibit a nonlinear collapse mode associated with the interaction of nearly equal linear bifurcation modes, for load levels below approximately 1.9 times the operational load level. However, the results do predict that the severity of some of the local deformations is significantly affected by the localized initial geometric imperfection.

References

[1]Nemeth, M. P., Britt, V. O., Collins, T. J., and Starnes, J. H., Jr., Nonlinear Analysis of the Space Shuttle Superlightweight External Fuel Tank, NASA TP 3616, December, 1996.

[2]Brogan, F. A., Rankin, C. C., and Cabiness, H. D., "STAGS User Manual," Lockheed Palo Alto Research Laboratory, Report LMSC P032594, 1994.

[3]Young, R. D. and Rankin, C. C., "Modeling and Nonlinear Analyses of a Large-Scale Launch Vehicle Under Combined Thermal and Mechanical Loads," Proceedings of the 37th AIAA/ASME/ASCE/AHS/ASC Structures, Structural Dynamics, and Materials Conference, Salt Lake City, Utah, April 15-17, 1996, pp. 2023-2033. AIAA Paper No. 96-1551

[4]Bushnell, D., "Static Collapse: A Survey of Methods and Modes of Behavior," Collapse Analysis of Structures, PVP-Vol. 84, ASME, 1984, pp. 30-32.

[5]Stephens, W. B., Starnes, J. H., Jr., and Almroth, B. O., "Collapse of Long Cylindrical Shells Under Combined Bending and Pressure Loads," *AIAA Journal*, Vol. 13, No. 1, 1975, pp. 20-25.